Three-Dimensional Nanobranched Indium–Tin-Oxide Anode for Organic Solar Cells

Hak Ki Yu,[†] Wan Jae Dong,[†] Gwan Ho Jung, and Jong-Lam Lee*

Division of Advanced Materials Science and Department of Materials Science and Engineering, Pohang University of Science and Technology (POSTECH), Pohang, 790-784, Korea. [†]These authors contributed equally to this work.

ABSTRACT A nanostructured three-dimensional (3D) electrode using transparent conducting oxide (TCO) is an effective approach for increasing the efficiency of optoelectronic devices used in daily life. Tin-doped indium oxide (ITO) is a representative TCO with high conductivity and a high work function for anode applications. This paper reports the fabrication of a large-area ITO nanostructure with a branch shape using an electron beam evaporation process at temperatures as low as 80 °C, which was free of any carrier gas and catalyst. The large surface to volume ratio in the anode by the ITO nanobranches increases both the hole mobility by a 3D pathway and light absorbance by scattering, resulting in organic solar cells with a 12% increase in photocurrent and 20% photoconversion efficiency based on the bulk heterojunction of P3HT [region-regular poly(3-hexylthiophene)] and PCBM [phenyl-C61-butyric acid methyl ester].

KEYWORDS: ITO · nanobranches · self-catalyst · electron beam evaporation · organic solar cells

Transparent conducting oxides (TCOs) based on bixbyite In_2O_3 (Sn-doped In_2O_3, ITO) and wurtzite ZnO (Al-, In-, and Ga-doped ZnO) are key materials for high-efficiency optoelectronic devices, such as light-emitting diodes, solar cells, and display panels.[1−7] Because a nanostructured three-dimensional (3D) TCO can increase not only the carrier mobility due to the high crystallinity of nanocrystals but also the optical path length due to randomly diffused light, many studies have been attempted to improve the efficiency of optoelectronic devices.[8−12] ZnO-based nanorods were grown using a low-cost and large-area growth technique based on zinc nitrate hexahydrate ($Zn(NO_3)_2 \cdot 6H_2O$) and methenamine ($C_6H_{12}N_4$).[8−11] However, ZnO-based materials have demerits, such as relatively higher resistivity (~10^{-4} Ωcm) than ITO (~10^{-5} Ωcm)[13,14] and weakness in acid-based processes.[15] Above all, the low work function (~4.0 eV) of ZnO is unsuitable for increasing the inherent low mobility of the hole in anode applications.[16,17]

The ITO nanostructure is certainly the most important issue for optoelectronic applications, owing to high conductivity, relatively stability in acidic atmospheres, and high work function (4.5−4.8 eV) for anode applications.[16,17] However, there have been few studies of the ITO nanostructure due to the complexity of the ternary composition system.[18] Although a few studies on ITO nanostructures based on a bottom-up approach have been attempted, the precise growth mechanism is still unclear, and the high growth temperature and poor uniformity are unsuitable for large-area applications in optoelectronic devices.[19−22] Typically, ITO nanostructures are synthesized by a vapor−liquid−solid (VLS) process using vapor phase epitaxy on Au-coated[19,20] or catalyst-free (self-catalyst) substrates by heating a mixture of In_2O_3, SnO_2, and graphite powder.[21,22] In both cases, the substrate is heated to more than 800 °C to maintain the liquid Au phase and the carbo-thermal reaction between graphite powder and In_2O_3 and SnO_2. Moreover, the byproduct induced by Au and graphite, such as AuIn, $AuIn_2$, and metal carbonate, can degrade the quality of the ITO nanostructures.[23] Meanwhile, most metal oxides could be decomposed easily by high-density beam energy, such as electron beam, and sufficient metal flux for the self-catalyst of the VLS process can be formed under a low oxygen partial pressure. In this case, VLS growth can be achieved easily just above the melting point of the metallic self-catalyst.

Here, we first report the large-area ITO nanostructure growth with a branch shape using an electron beam evaporation process, which is free of any carrier gas and catalyst (Figure 1a). Organic solar cells (OSCs) using the ITO nanobranches as a 3D anode (Figure 1b) exhibited outstanding device performance due to the enhanced hole mobility, perfect wetting of the polymers

* Address correspondence to jllee@postech.ac.kr.

Received for review July 11, 2011 and accepted September 7, 2011.

Published online September 07, 2011
10.1021/nn2025836

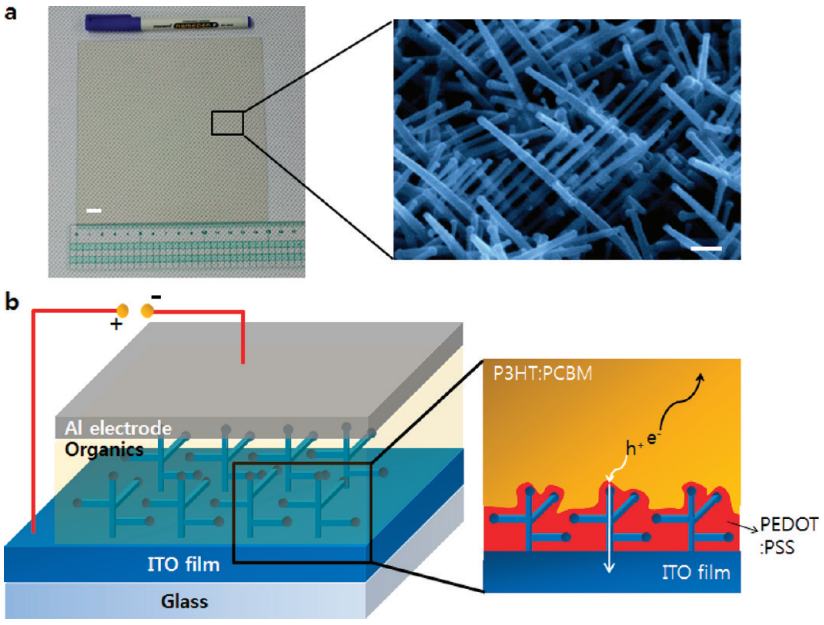

Figure 1. (a) Camera image of uniformly deposited ITO nanostructures on ITO-coated glass over a large area (15 cm × 15 cm). Scale bar, 10 cm. The enlarged SEM image clearly shows the ITO nanobranches. Scale bar, 100 nm. The ITO nanostructure was grown at 300 °C during 6 min at a rate of 0.5 nm/s. (b) Schematic view of 3D ITO nanobranch applied OSC devices. PEDOT:PSS is coated on the ITO nanobranches and the P3HT:PCBM bulk heterojunction was used as the active layer. The thermally evaporated Al layer was selected as a cathode.

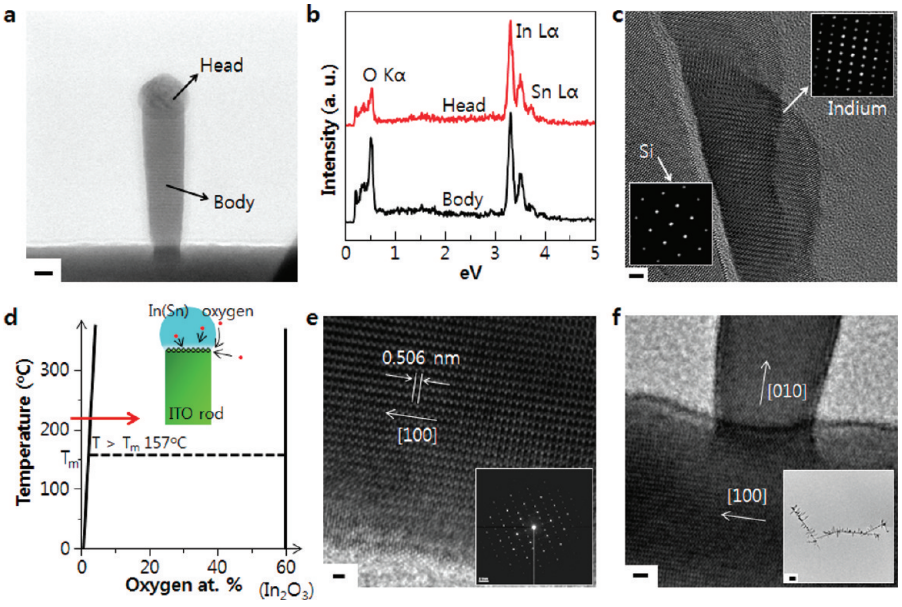

Figure 2. (a) TEM image of a single ITO nanorod grown on Si(100) substrate at 300 °C, indicating the existence of a spherical VLS head. Scale bar, 10 nm. (b) EDS results of the head and body of an ITO nanorod shown in (a). Significant increase in oxygen Kα in the body area due to ITO formation from the metallic In(Sn) head by the VLS process. (c) High-resolution TEM image at the initial stage of growth and Fourier transformed diffraction patterns (inset) of the sample grown 10 s at 300 °C on Si(100), indicating a well-crystallized tetragonal metallic indium phase. Scale bar, 2 nm. (d) In−O phase diagram and growth mechanism of ITO nanorod by VLS. Over the melting point of an In(Sn) nanodot (157 °C for the pure indium at bulk status), the continuous supply of oxygen into the nanodot causes the segregation of a supersaturated In_2O_3 phase according to the lever rule. (e) HR-TEM image and electron diffraction pattern (inset), indicating a well-crystallized ITO with (100) orientation d = 0.506 nm. Scale bar, 1 nm. (f) HR-TEM image in the junction of the ITO nanobranch with a 90° tilted angle by (100) and (010) orientations. Scale bar, 2 nm. The inset is the TEM image of the ITO nanobranch transferred carbon film coated Cu grid. Scale bar, 200 nm.

by Wenzel's contact mode,[24] and the long path length of the photon by scattering, resulting in a 12% increase in photocurrent and 20% photoconversion efficiency. This acts as a key step in the development of high-efficiency optoelectronic devices for future generations.

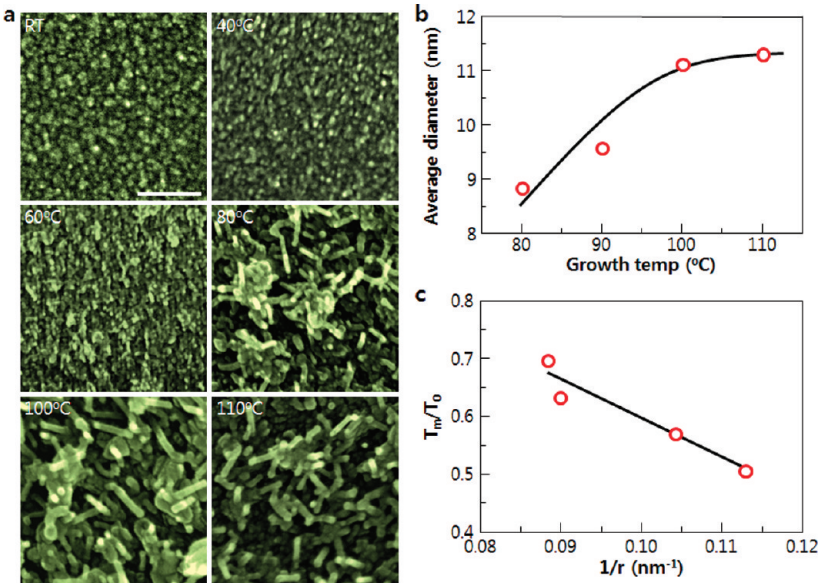

Figure 3. (a) Top-view SEM images of the deposited ITO surface grown on Si(100) substrate with respect to the growth temperature from room temperature to 110 °C. The growth time was set at about 6 min at the rate of 0.5 nm/s. Scale bar, 100 nm. (b) Mean diameter size of In(Sn) nanodot with respect to growth temperature. (c) $d(T_m/T_0)/d(1/r)$ plot of the In(Sn) nanodot during the VLS process.

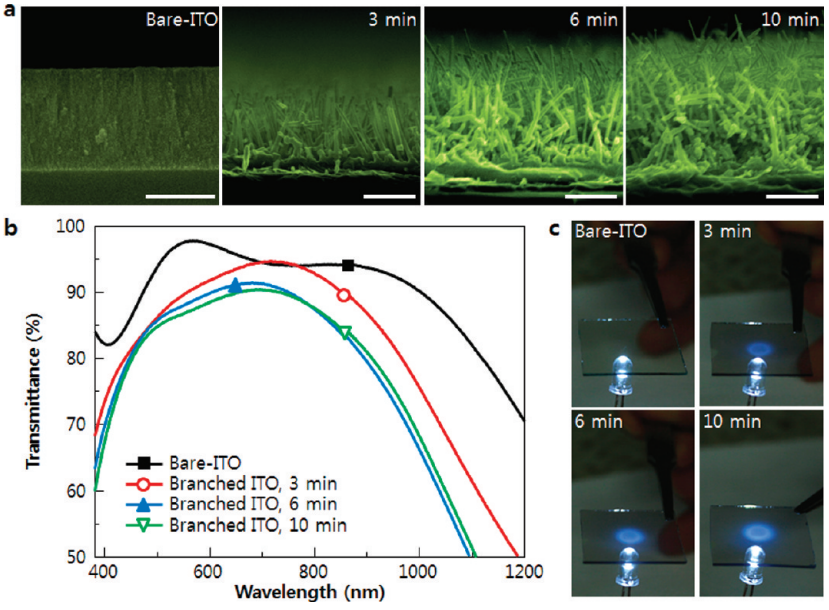

Figure 4. (a) Cross-section SEM images of bare-ITO film and nanobranched ITO grown on Si(100) substrate at 300 °C during 3, 6, and 10 min (rate = 0.5 nm/s). Scale bar, 100 nm. (b) Transmittance of ITO nanobranches from 380 to 1200 nm at different growth times grown on soda-lime glass. (c) Photographs of scattered light by the ITO nanobranches using YAG phosphor conversed conventional GaN white LEDs (injected current was set as constant 1 mA).

RESULTS AND DISCUSSION

A number of metallic microdroplets were produced at the surface of the electron-beam-irradiated ITO pellet (Supplementary Figure S1). The growth of self-assembled ITO nanorods can be achieved by evaporating those metallic droplets and forming a tin-alloyed indium [In(Sn)] nanodot. The In(Sn) nanodots were distributed uniformly with several tens of nanometer size at the initial stages of growth, and the detailed composition of the In(Sn) nanodot was confirmed by Auger spectroscopy (Supplementary Figure S2). Because In(Sn) alloy is a eutectic system (eutectic point of atomic concentration: 52% indium and 48% tin),[25] the melting point decreased with increasing tin composition in the In(Sn) alloy, resulting in the easy formation of a liquid phase nanodot. Those dots gradually transformed to nanorod structures with a spherical head (Figure 2a). The significant color contrast in the

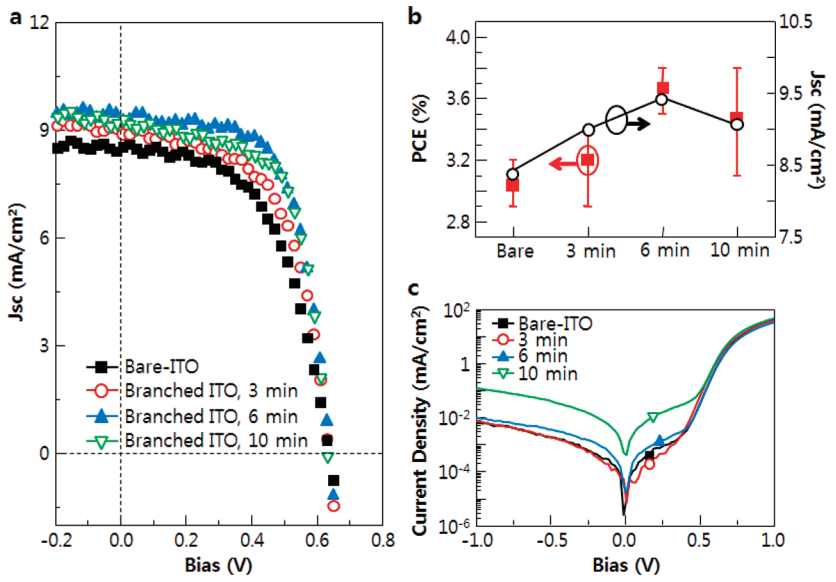

Figure 5. (a) Current density *versus* voltage ($J-V$) characteristics. The short-circuit current (J_{sc}) was higher for the samples with ITO nanorods (9.0 mA/cm^2 for 3 min growth, 9.4 mA/cm^2 for 6 min growth, and 9.1 mA/cm^2 for 10 min growth) than the planar ITO film (8.4 mA/cm^2). (b) PCE (solid red squares) and J_{sc} (open black circles) properties of the OSCs. The average PCE increases from 3.03% for bare-ITO film to 3.20% (ITO nanorods grown 3 min), 3.67% (6 min), and 3.47% (10 min). (c) Dark current characteristics. The leakage current appeared for the long length of the ITO nanobranch sample (10 min). Detailed device parameters are summarized in Table 1.

EELS maps (Supplementary Figure S3), the difference in oxygen composition between the head and body of the nanorod (Figure 2b), and HR-TEM images (Figure 2c) confirm the nucleation of metallic nanodots at the initial growth stage. After In(Sn) nanodot formation, oxygen molecules from the electron-beam-irradiated ITO pellet dissolved into the head of the In(Sn) nanodot. The oxygen solubility in In(Sn) is extremely low (0.5 at. % at 1000 °C),[26] leading to the formation of ITO at the bottom of the nanodot.[27] As a result, the ITO nanorods were grown through the successive supplementation of oxygen atoms from the surrounding vacuum chamber (Figure 2d). The fabricated ITO nanorods showed a well-aligned bixbyite single crystal In_2O_3 (100) orientation (Figure 2e and inset). The nanorods had a specific branch shape with a 90° rotation angle. In the junction of the branch, continuous atomic arrangement could be confirmed with the {100} family plane orientation of cubic based bixbyite In_2O_3 (Figure 2f and inset). The orientation of the ITO nanobranch was clearly confirmed using a Fourier filtering process by masking the {100} Fourier transformed diffraction patterns (Supplementary Figure S4a). The bright region in the Fourier filtered image shows the orientation of the {100} family plane in the ITO nanobranch structure. The In_2O_3 {100} family planes, such as (100), (010), and (001), have metallic indium termination. Therefore, the In(Sn) self-catalyst could be formed easily at those planes, resulting in a nanobranch structure with a 90° rotation angle, as shown in Supplementary Figure S4b.

Figure 3a shows the top-view SEM images of the ITO surface with respect to the growth temperature. The ITO nanorod structure was formed spontaneously above 80 °C. The melting point of pure indium metal is about 157 °C. Although the eutectic alloy of indium and tin could reduce the melting point of indium by up to 120 °C, a liquid phase could not exist in the bulk status near 80 °C. However, the melting point of the nanodot is lower than the bulk, resulting in a VLS process, even at 80 °C.[28,29] The size of the In(Sn) nanodot increased with increasing growth temperature because the melting point is proportional to the size of the nanodot on the nanoscale (Figure 3b). In classical thermodynamics, the melting point of nanoparticles (T_m) is defined as[28]

$$\frac{T_m}{T_0} = 1 - \frac{3(\sigma_s/\rho_s - \sigma_l/\rho_l)}{l_0 r}$$

where T_0 is the bulk melting temperature, r is the particle radius, l_0 is the latent heat per unit mass, σ_s and σ_l are the specific surface energies of the solid and liquid, respectively, and ρ_s and ρ_l are the densities of the solid and liquid, respectively. Generally the pure indium has a slope defined as $d(T_m/T_0)/d(1/r)$ in the range of about −0.29 to −1.05.[28] However, the slope was calculated to be about −6.71 in our experimental results due to the tin alloying and high-vacuum conditions during growth (Figure 3c). Although the change in In(Sn) nanodot size had an effect on the diameter of the ITO nanorod, the length of the ITO nanorod was more critically affected by the growth temperature due to the change in solubility of oxygen in the In(Sn) nanodot. Because the solubility of oxygen in the In(Sn) nanodot increases with growth temperature, the long length of the ITO nanorod appeared as the growth

temperature increased. So, we used the growth temperature of about 300 °C for the well-developed ITO nanostructure application in OSCs (Supplementary Figure S5).

As the ITO nanorods continued to grow, they showed a more linked and branched structure with a pine-tree-like appearance due to additional In(Sn) nanodot nucleation on the {100} family plane of the bixbyite crystal (Figure 4a). Although the transmittance of the ITO nanobranch was slightly lower than the bare-ITO film (Figure 4b), there was no severe loss in spectral irradiance in the 450−600 nm region, where the absorbance of the P3HT:PCBM active layer appears (Supplementary Figure S6).[30] Moreover, a light-scattering effect was not observed in the bare-ITO film, whereas samples with the ITO nanobranches showed a clear ring pattern, indicating the scattering of light. As the growth time of the ITO nanorods increased, the scattered ring pattern became larger and clearer due to the high density and developed nanobranch structures, as shown in Figure 4c. The scattering characteristics of the ITO nanobranch could increase the photon path length in the active layer of the OSCs, resulting in a high-performance device.

The current density−voltage (J−V) curves indicate the increase in short-circuit current (J_{sc}) for the samples with ITO nanobranches compared to the planar ITO film (Figure 5a). The increase in J_{sc} can be explained by three reasons. First, the single-crystalline ITO nanobranches act as direct conducting pathways for hole transport, resulting in a charge balance between the hole and electron. This charge balance prevents charge recombination losses and increases the photocurrent.[31,32] Second, enhanced absorption in the P3HT:PCBM active layer was achieved using these ITO nanostructures. The ITO nanostructures diffused the incident light and inclined the injection angle of the photons, resulting in an increase in the distance of the photon passing through the active layer. Third, the nanobranch structures improved the coverage of poly(3,4-ethylenedioxythiophene) poly(styrenesulfonate), PEDOT:PSS, on ITO (Supplementary Figure S7). In Wenzel's equation, the contact angle decreases with increasing surface roughness, resulting in a superhydrophilic surface.[24] The conformal wetting of PEDOT:PSS on ITO nanorods increases the hole extraction to the ITO anode. The average photoconversion efficiency (PCE) increased by adapting ITO nanobranch structures (Figure 5b). The PCE tendency was well matched with the J_{sc} characteristics, which confirmed that the length of the ITO nanobranches affects the device performance. The decrease in PCE for the sample with the ITO nanobranches grown for 10 min could be explained by leakage current. As the growth time of ITO increased, the ITO nanobranches with an abnormally long length could be grown, resulting in the generation of leakage current (Figure 5c). The leakage current degraded the device performance and decreased the PCE.

TABLE 1. Device Parameters with Respect to Growth Time

	J_{SC} (mA/cm^2)	V_{OC} (V)	FF (%)	PCE (%)
bare ITO	8.4	0.633	57	3.03
3 min	9	0.633	56.2	3.2
6 min	9.4	0.633	61.7	3.67
l0 min	9.1	0.633	60.2	3.47

Compared with the conventional method of ITO nanorod fabrication, the electron beam evaporation method has several merits. First, the simple and large-area growth process of ITO nanorods has a great advantage for large-area applications at a low cost. Second, the growth temperature of the VLS process using a self-catalyst In(Sn) nanodot could be reduced to as low as the melting point of the In(Sn) nanodot. Experimentally, the minimum growth temperature was as low as 80 °C. However, the additional sufficient growth temperature over 200 °C was needed for the highly efficient OSCs device due to low transparency and the short length of the ITO nanostructures (Supplementary Figure S8). Third, ITO nanorods could be grown independent of the substrate type, even though the surface energy of the substrate affected the density of the In(Sn) nanodots at the initial growth stage (Supplementary Figure S9). In conclusion, this paper reports the growth of ITO nanorods with a branch structure by electron beam evaporation, opening the possibility of large-area optical device applications, particularly PSCs based on the bulk heterojunction of P3HT and PCBM. The large surface to volume ratio in the anode by the ITO nanobranches increases the hole mobility *via* a 3D pathway as well as the light absorbance by light scattering at any time, resulting in an increase in photoconversion efficiency from 3.03% to 3.67%. The ITO nanostructure fabricated in this study could be used in other optical devices, such as inorganic solar cells, light-emitting diodes, and laser diodes due to the large-area growth characteristics and easy fabrication method.

CONCLUSION

In conclusion, an ITO nanostructure with a branch shape has been successfully fabricated using the electron beam evaporation method at temperatures as low as 80 °C, which was free of any carrier gas and catalyst. By using these experimental results, we could overcome the demerits of the conventional method for producing ITO nanostructures such as small area, high temperatures, over 800 °C, and contamination by catalyst. The self-catalytic In(Sn) nanodot was spontaneously formed by an electron beam irradiated ITO pellet, resulting in a VLS process for ITO nanobranch growth just over the melting point of the In(Sn) nanodot. The large surface to volume ratio in the

anode by the ITO nanobranches increases both the hole mobility by a 3D conducting pathway and light absorbance by scattering, resulting in organic solar cells with a 12% increase in photocurrent and 20% photoconversion efficiency based on the bulk heterojunction of P3HT:PCBM.

METHODS

Self-assembled ITO nanobranches were fabricated by an electron beam evaporation method. A tin-doped (10%) indium oxide pellet (99.99%) was used as the source material. ITO nanobranches were grown at a rate of 0.5 nm s^{-1}. However, the growth rate was not linear due to the development of branch structure with growth time. The chamber pressure was maintained at approximately 10^{-5} Torr during deposition, and the substrate temperature was held at 300 °C for the well-developed ITO nanobranches. SEM was done using a PHILIPS XL30S with an accelerating voltage of 10 kV and a working distance of 5 mm. The HR-TEM images were collected using a Cs-corrected JEM 2200FS operated at 200 kV. AES was measured by a VG Scientific MICROLAB310F with a minimum beam size of 15 nm and a 0.05% energy resolution. High-resolution spectromicroscopy using synchrotron radiation was carried out at the 8A1 beamlines at Pohang Accelerator Laboratory, and the space resolution was 0.5 μm. Atomic force microscopy images were recorded using a Digital Instruments Nanoscope III in tapping mode using silicon cantilevers. The transmittance was measured using a tungsten-halogen lamp and a monochromator.

The OSC devices were fabricated as below. Glass coated with ITO (160 nm thick, ~15 Ω/sq) was used as the starting substrate. After the growth of ITO nanobranches, the substrates were cleaned using a UV−O treatment for 15 min with a power of 30 mW/cm^2. Subsequently, PEDOT:PSS was spin-coated and dried at 200 °C for 10 min. After the PEDOT:PSS coating, the substrates were transferred to a N_2-filled glovebox (<0.1 ppm O_2 and H_2O). Regioregular poly(3-hexylthiophene) (P3HT, purchased from Rieke Metals and used as received) was first dissolved in 1, 2-dichlorobenzene to make a 20 mg/mL solution, followed by blending with phenyl-C61-butyric acid methyl ester (PCBM, Nano-C, used as received) in a 1:1 weight ratio. The blend was stirred for ~14 h in a glovebox before being spin-coated (700 rpm, 30 s) on the top of the PEDOT:PSS layer. The active layer thickness was measured to be ~200 nm using a surface profiler. The devices were annealed on a hot plate in a glovebox at 130 °C for 10 min. The cathode consisted of LiF (ca. 1 nm) coated with Al (ca. 100 nm), which was deposited at a base pressure of 2×10^{-6} Torr by thermal evaporation method. The active device area was ca. 0.04 cm^2. The $J-V$ curves were measured under ambient air with glass encapsulation using a Keithley 2400 source measurement unit. The photocurrent was measured under AM1.5G 100 mW cm^{-2} illumination using an Oriel 150 W solar simulator. The light intensity was determined using a monosilicon detector calibrated by the National Renewable Energy Laboratory. For accurate measurements of the device performance, only the active area of the samples was exposed.

Acknowledgment. This study was supported in part by the Priority Research Centers Program through the National Research Foundation of Korea (NRF) funded by the Ministry of Education, Science and Technology (2010-0029711) and in part by the WCU (World Class University) program through the Korea Science and Engineering Foundation funded by the Ministry of Education, Science and Technology (Project No. R31-2008-000-10059-0).

Supporting Information Available: This material is available free of charge *via* the Internet at http://pubs.acs.org.

REFERENCES AND NOTES

1. Reineke, S.; Lindner, F.; Schwartz, G.; Seidler, N.; Walzer, K.; Lussem, B.; Leo, K. White Organic Light-Emitting Diodes with Fluorescent Tube Efficiency. *Nature* **2009**, *459*, 234–238.
2. Campoy-quiles, M.; Ferenczi, T.; Agostinelli, T.; Etchegoin, P. G.; Kim, Y.; Anthopoulos, T. D.; Stavrinou, P. N.; Bradley, D. D. C.; Nelson, J. Morphology Evolution *via* Self-Organization and Lateral and Vertical Diffusion in Polymer: Fullerene Solar Cell Blends. *Nat. Mater.* **2008**, *7*, 158–164.
3. Caruge, J. M.; Halpert, J. E.; Wood, V.; Bulović, V.; Bawendi, M. G. Colloidal Quantum-Dot Light-Emitting Diodes with Metal-Oxide Charge Transport Layers. *Nat. Photonics* **2008**, *2*, 247–250.
4. Sun, Y.; Forrest, S. R. Enhanced Light Out-Coupling of Organic Light-Emitting Devices Using Embedded Low-Index Grids. *Nat. Photonics* **2008**, *2*, 483–487.
5. Park, S. H.; Roy, A.; Beaupré, S.; Cho, S.; Coates, N.; Moon, J. S.; Moses, D.; Leclerc, M.; Lee, K.; Heeger, A. J. Bulk Heterojunction Solar Cells with Internal Quantum Efficiency Approaching 100%. *Nat. Photoics.* **2009**, *3*, 297–302.
6. Yip, H.-L.; Hau, S. K.; Baek, N. S.; Ma, H.; Jen, A. K.-Y. Polymer Solar Cells That Use Self-Assembled-Monolayer-Modified ZnO/Metals As Cathodes. *Adv. Mater.* **2008**, *20*, 2376–2382.
7. Yuan, G.-D.; Zhang, W.-J.; Jie, J.-S.; Fan, X.; Tang, J.-X.; Shafiq, I.; Ye, Z.-Z.; Lee, C.-S.; Lee, S.-T. Tunable n-Type Conductivity and Transport Properties of Ga-doped ZnO Nanowire Arrays. *Adv. Mater.* **2008**, *20*, 168–173.
8. Law, M.; Greene, L. E.; Johnson, J. C.; Saykally, R.; Yang., P. Nanowire Dye-Sensitized Solar Cells. *Nat. Mater.* **2005**, *4*, 455–459.
9. Yan, R.; Gargas, D.; Yang., P. Nanowire Photonics. *Nat. Photonics* **2009**, *3*, 569–576.
10. Greene, L. E.; Law, M.; Yuhas, B. D.; Yang, P. ZnO−TiO_2 Core−Shell Nanorod/P3HT Solar Cells. *J. Phys. Chem. C* **2007**, *111*, 18451–18456.
11. Lin, Y.-Y.; Chen., C.-W.; Chu, T.-H.; Su, W.-F.; Lin, C.-C.; Ku, C.-H.; Wu, J.-J.; Chen, C.-H. Nanostructured Metal Oxide/Conjugated Polymer Hybrid Solar Cells by Low Temperature Solution Processes. *J. Mater. Chem.* **2007**, *17*, 4571–4576.
12. O'Dwyer, C.; Szachowicz, M.; Visimberga, G.; Lavayen, V.; Newcomb, S. B.; Torres, C. M. S. Bottom-Up Growth of Fully Transparent Contact Layers of Indium Tin Oxide Nanowires for Light-Emitting Devices. *Nat. Nanotechnol.* **2009**, *4*, 239–244.
13. Papadopoulou, E. L.; Varda, M.; Kouroupis-Agalou, K.; Androulidaki, M.; Chikoidze, E.; Galtier, P.; Huyberechts, G.; Aperathitis, E. Undoped and Al-doped ZnO Films with Tuned Properties Grown by Pulsed Laser Deposition. *Thin Solid Films* **2008**, *516*, 8141–8415.
14. Lee, J. Y.; Jang, B. R.; Lee, J. H.; Kim, H. S.; Cho, H. K.; Moon, J. Y.; Lee, H. S.; Lee, W. J.; Baek, J. W. Characterization of Low Mole Fraction In-doped-ZnO/Si (111) Heterostructure Grown by Pulsed Laser Deposition. *Thin Solid Films* **2009**, *517*, 4086–4089.
15. Chou, T. P.; Zhang, Q.; Cao, G. Effects of Dye Loading Conditions on the Energy Conversion Efficiency of ZnO and TiO_2 Dye-Sensitized Solar Cells. *J. Phys. Chem. C* **2007**, *111*, 18804–18811.
16. Wenckstern, H.; von; Biehne, G.; Rahman, R. A.; Hochmuth, H.; Lorenz, M.; Grundmann, M. Mean Barrier Height of Pd Schottky Contacts on ZnO Thin Films. *Appl. Phys. Lett.* **2006**, *88*, 092102.
17. Kim, H.; Gilmore, C. M.; Horwitz, J. S.; Piqué, A.; Murata, H.; Kushto, G. P.; Schlaf, R.; Kafafi, Z. H.; Chrisey, D. B. Transparent Conducting Aluminum-Doped Zinc Oxide Thin Films for Organic Light-Emitting Devices. *Appl. Phys. Lett.* **2000**, *76*, 259–261.
18. Peng, X. S.; Meng, G. W.; Wang, X. F.; Wang, Y. W.; Zhang, J.; Liu, X.; Zhang, L. D. Synthesis of Oxygen-Deficient Indium−Tin-Oxide (ITO) Nanofibers. *Chem. Mater.* **2002**, *14*, 4490–4493.

19. Wan, Q.; Dattoli, E. N.; Fung, W. Y.; Guo, W.; Chen, Y.; Pan, X.; Lu, W. Fully Transparent Thin-Film Transistor Devices Based on SnO_2 Nanowires. *Nano Lett.* **2006**, *6*, 2909–2915.
20. Jang, H. S.; Kim, D.-H.; Lee, H.-R.; Lee, S.-Y. Field Emission From Cone-Like Single Crystalline Indium Tin Oxide Nanorods. *Mater. Lett.* **2005**, *59*, 1526–1529.
21. Xue, X. Y.; Chen, Y. J.; Liu, Y. G.; Shi, S. L.; Wang, Y. G.; Wang, T. H. Synthesis and Ethanol Sensing Properties of Indium-Doped Tin Oxide Nanowires. *Appl. Phys. Lett.* **2006**, *88*, 201907.
22. Chiquito, A. J.; Lanfredi, A. J. C.; Leite, E. R. One-Dimensional Character of Sn Doped In_2O_3 Nanowires Probed by Magnetotransport Measurements. *J. Phys. D: Appl. Phys.* **2008**, *41*, 045106.
23. Okamoto, H. Au-In (Gold-Indium). *J. Phase Equilib. Diffus.* **2004**, *25*, 197–198.
24. Wenzel, R. N. Surface Roughness and Contact Angle. *J. Phys. Chem.* **1949**, *53*, 1466–1467.
25. Okamoto, H. In-Sn (Indium-Tin). *J. Phase Equilib. Diffus.* **2004**, *27*, 313.
26. Okamoto, H. In-O (Indium-Oxygen). *J. Phase Equilib. Diffus.* **2007**, *28*, 591–592.
27. Oh, S. H.; Chisholm, M. F.; Kauffmann, Y.; Kaplan, W. D.; Luo, W.; Ruhle, M.; Scheu, C. Oscillatory Mass Transport in Vapor-Liquid-Solid Growth of Sapphire Nanowires. *Science* **2010**, *330*, 489–493.
28. Allen, G. L.; Bayles, R. A.; Gile, W. W.; Jesser, W. A. Small Particle Melting of Pure Metals. *Thin Solid Films* **1986**, *144*, 297–308.
29. Xie, D.; Wang, M. P.; Qi, W. H.; Cao, L. F. Thermal Stability of Indium Nanocrystals: A Theoretical Study. *Mater. Chem. Phys.* **2006**, *96*, 418–421.
30. Kim, J. Y.; Lee, K.; Coates, N. E.; Moses, D.; Nguyen, T.; Dante, M.; Heeger, A. J. Efficient Tandem Polymer Solar Cells Fabricated by All-Solution Processing. *Science* **2007**, *317*, 222–225.
31. Mihailetchi, V. D.; Xie, H.; Boer, B.; de; Koster, L. J. A.; Blom, P. W. M. Charge Transport and Photocurrent Generation in Poly(3-hexylthiophene):Methanofullerene Bulk-Heterojunction Solar Cells. *Adv. Funct. Mater.* **2006**, *16*, 699–708.
32. Choulis, S. A.; Nelson, J.; Kim, Y.; Poplavskyy, D.; Kreouzis, T.; Durrant, J. R.; Bradley, D. D. C. Investigation of Transport Properties in Polymer/Fullerene Blends Using Time-of-Flight Photocurrent Measurements. *Appl. Phys. Lett.* **2003**, *83*, 3812–3814.